

Article

Petrography and Shock Metamorphism of the Lunar Breccia Meteorite NWA 13120

Zhipeng Xia ^{1,2} , Bingkui Miao ^{1,2,*} , Chuantong Zhang ^{1,2,3}, Hongyi Chen ^{1,2}, Lanfang Xie ^{1,2}, P. M. Ranjith ⁴, Yikai Zhang ^{1,2} and Bowen Si ^{1,2}

- ¹ Guangxi Key Laboratory of Hidden Metallic Ore Deposits Exploration, Guilin University of Technology, Guilin 541006, China; xiazhipeng@glut.edu.cn (Z.X.); zct@glut.edu.cn (C.Z.); chy@glut.edu.cn (H.C.); 6615012@glut.edu.cn (L.X.); zhangyikai1996@outlook.com (Y.Z.); szebown@outlook.com (B.S.)
- ² Institution of Meteorites and Planetary Materials Research, College of Earth Sciences, Guilin University of Technology, Guilin 541006, China
- ³ Key Laboratory of Lunar and Deep Space Exploration, Chinese Academy of Sciences, Beijing 100029, China
- ⁴ Key Laboratory of Earth and Planetary Physics, Institute of Geology and Geophysics, Chinese Academy of Sciences, Beijing 100029, China; ranjith@mail.iggcas.ac.cn
- * Correspondence: miaobk@glut.edu.cn

Abstract: Lunar meteorites are the fragments of rocks that fell on Earth because of the impacts of asteroids on the Moon. Such rocks preserve information about the composition, evolutionary process, and shock history of the lunar surface. NWA 13120 is a recently discovered lunar breccia meteorite having features of strong shock, which is composed of lithic and mineral clasts in a matrix of very fine-grained (<10 μm) and recrystallized olivine-plagioclase with a poikilitic-like texture. As the most abundant lithic clasts, the crystalline impact melt (CIM) clasts can be divided into four types according to their texture and mineral composition: (1) anorthosites or troctolitic anorthosite with a poikilitic-like texture, but the mineral content is different from that of the matrix; (2) anorthosites containing basaltic fragments and rich in vesicles; (3) troctolitic anorthosite containing metamorphic olivine mineral fragments; (4) troctolitic anorthosite containing troctolite fragments. Based on the petrology and mineralogy, NWA 13120 is a lunar meteorite that was derived from the ferrous anorthosite suite (FANs) of the lunar highlands, while its texture suggests it is a crystalline impact melt breccia. In addition, we infer that the parent rock of NWA 13120 is a lunar regolith breccia enriched in glass fragments. During the shock process, at pressures of more than 20 GPa, all plagioclase fragments were transformed into maskelynites, and olivine fragments occurred metamorphism. The post-shock temperature led to the partial melting of the basaltic fragments. Subsequently, all glass with diverse components in the parent rock were devitrified and recrystallized, forming the common olivine-plagioclase poikilitic-like texture and different CIM clasts. Meanwhile, the devitrification of maskelynite formed the accumulation of a large number of plagioclase microcrystals. Therefore, NWA 13120 is a meteorite of great significance for understanding the local shock metamorphism of lunar rocks on the lunar surface.

Keywords: lunar meteorite; NWA 13120; breccia; shock metamorphism; devitrification



Citation: Xia, Z.; Miao, B.; Zhang, C.; Chen, H.; Xie, L.; Ranjith, P.M.; Zhang, Y.; Si, B. Petrography and Shock Metamorphism of the Lunar Breccia Meteorite NWA 13120. *Minerals* **2021**, *11*, 899. <https://doi.org/10.3390/min11080899>

Academic Editors: Ioannis Baziotis and Roman Skála

Received: 16 May 2021

Accepted: 12 August 2021

Published: 20 August 2021

Publisher's Note: MDPI stays neutral with regard to jurisdictional claims in published maps and institutional affiliations.



Copyright: © 2021 by the authors. Licensee MDPI, Basel, Switzerland. This article is an open access article distributed under the terms and conditions of the Creative Commons Attribution (CC BY) license (<https://creativecommons.org/licenses/by/4.0/>).

1. Introduction

Although about 382 kg of lunar samples were obtained during the Apollo, Luna and Chang'E missions, these samples were collected only in the small areas of the near side of the Moon [1,2]. In contrast, lunar meteorites are the materials randomly ejected from the surface of the Moon, which can be more representative of material from the entire Moon [3,4]. At present, although more than 470 lunar meteorites have been collected (Meteoritical Society: <https://meteoritical.org/>, date accessed: 12 August 2021), the number is still very small. According to global remote sensing data, the lunar surface is generally composed of highland anorthosite, mare basalt, and rocks rich in KREEP components

(Potassium, Rare Earth Elements, and Phosphorus) [4]. The breccias are formed from a variety of rocks, minerals, and glassy materials, and they are widely distributed on the surface of the Moon, of which anorthosite breccia meteorites account for about two-thirds of all recovered lunar meteorites (Meteoritical Society: <https://meteoritical.org/>, date accessed: 12 August 2021). The petrological and geochemical analyses of anorthosite breccia meteorites show that their composition is more complex than that of highland anorthosite meteorites [5,6]. Because of the complexity of lunar breccia composition (materials from different lunar regions, multi-stage shock sputtered materials, and complex rock fragments), it is often difficult to accurately determine the initial location of the samples. However, by understanding the composition of the breccia meteorites, we can constrain their source region and metamorphism (e.g., [7–10]). The large numbers of impact craters and the several-meters-thick lunar soil layer show that the lunar crust has experienced a large number of meteor impacts [11]. The shock process has altered the overall texture of the lunar meteorites, which record important information about the shock events, and thus provides evidence about the metamorphism of the lunar rocks after the shock (e.g., [12–14]).

NWA 13120 is an anorthositic lunar breccia meteorite, weighing 819.04 g, which was found in Morocco in 2017. Preliminary analysis shows that this lunar breccia experienced strong shock and consists of a variety of impact melt clasts (Z. Xia, B. Miao, in *Meteoritical Bulletin*, no. 109, in preparation, 2020), which provide information for understanding the complex material composition of the Moon and the shock melting process. In this study, we analyze the mineralogical and petrological characteristics of the clasts and matrix in NWA 13120 and clarify the lithology of the clasts to promote the understanding of the composition of the lunar crust, the petrogenesis and the shock process.

2. Analytical Methods

The meteorite sample used for this study is the polished section (about 1 mm thick) made from NWA 13120, with dimensions of about 3.8 cm × 2.5 cm. All the analyses were performed at Guangxi Key Laboratory of Hidden Metallic Ore Deposits Exploration, Guilin University of Technology, China.

We used a Zeiss field emission scanning electron microscope to observe the petrology and acquire semi-quantitative mineral composition of NWA 13120. We then used a JEOL JXA-8230 electron probe with an acceleration voltage of 15 keV and a beam current of 20 nA for the quantitative mineral composition analysis. In order to reduce the influence of X-rays on K and Na elements, the analytical spot size for plagioclase was set to 3 μm, and the other minerals was set to 1 μm. Standards for these analyses were forsterite (SiKα, FeKα, MgKα), MnO₂ (MnKα), anorthite (AlKα), wollastonite (CaKα), albite (NaKα), phlogopite (KKα), rutile (TiKα), and apatite (PKα). These were made by the Institute of Geology and Geophysics, Chinese Academy of Sciences. The analysis results were corrected using the ZAF method [15]. Quantitative X-ray elemental mapping of basaltic fragments was performed with the same instrument. An area of 200 μm × 200 μm was chemically mapped. The analytical conditions were 0.5 μm beam and 0.5 μm step size, resulting X-ray maps with sizes of 400 × 400 pixels. Other test conditions of mapping scanning analysis are the same as mineral spot analysis.

We analyzed the bulk rock composition of NWA 13120 using the following two methods: (1) the electron probe defocusing method with stage scanning [6], where the current beam spot size was 100 μm, and multiple areas were selected for analysis by avoiding vesicles as much as possible; (2) 0.03 g of sample was placed in a platinum tube at a pressure of 5 kPa, heated to 1480 °C, and then rapidly cooled to obtain a molten bead of the sample, and subsequently the data were obtained by electron micro probe point analysis with glass as standard samples [16]. Although the content of Na and K in the method of measuring by molten bead may be low, the data obtained are very close with that obtained by the defocusing method (see Section 3.3). Since the content of Na and K is not high, the loss of Na and K may have little effect on the results.

In addition, Raman spectroscopy was employed to analyze the mineral phases. Using a Renishaw inVia Raman spectrometer, we measured the sample with a 514 nm Ar⁺ laser. When the laser reaches the surface of the sample, its power is approximately 10 mW. All the tests were performed under a 100 magnification and 0.85 numerical aperture objective lens with a laser focus of less than 1 μm . The spectral resolution was 1 cm^{-1} , and the Raman displacement test range was 100 to 1300 cm^{-1} [17]. Raman calibration was performed using monocrystal silicon wafers, where the Raman shift was 520.7 cm^{-1} .

The modal abundances of different minerals were determined by scaled pixel counting by delimiting color ranges within backscattered electron images by analysis of RGB histograms.

3. Petrography and Mineralogy of NWA 13120

The polished section of NWA 13120 is irregularly elliptical, with a noticeable brecciated texture (Figure 1). The clasts are largely composed of brown-black to brown-yellow lithic fragments and white to light-yellow plagioclase mineral fragments (>50 μm). The matrix is light yellow and consists of a large number of fine-grained minerals (<50 μm). The major mineral is plagioclase (~84.5 vol%), with minor amounts of olivine, spinel, chromite, pyroxene, ilmenite, and terrestrial weathering products (1.5 vol%, chiefly barite, with a small amount of calcite, quartz, potassium feldspar, and iron oxides).

3.1. Lithic Clasts

The different types of lithic clasts in the section of NWA 13120 generally include crystalline impact melt (CIM) clasts and two basaltic clasts. Their petrological and mineralogical characteristics are as follows.

3.1.1. Crystalline Impact Melt Clasts

The crystalline impact melt (CIM) clasts, as the most abundant lithic clasts in NWA 13120, which range in size from <100 μm to 3 mm (most are between 200 μm and 2 mm, where 113 pieces are larger than 300 μm) (Figure 1). Most of the clasts are round/subround, elliptical/subelliptical, with different numbers of vesicles and no clear edges or corners. The presence of two or more clasts gathered together leads to an irregular shape. From the composition and texture of the minerals, the CIM clasts can be divided into four types: 108 pieces in the first type, 3 pieces in the second type, and 1 piece in each of the other two types.

The first type of CIM clasts, accounting for the largest number, is represented by gray circles in Figure 1, for a total of 105 pieces. These clasts are composed of olivine-plagioclase assemblage with a poikilitic-like texture (Figure 2a). The plagioclases (>60 vol%, Raman spectrum is shown in Figure 3) are lath-shaped with different orientations, with a width of 1 to 5 μm (Figure 2(a-2,a-3)). The Anorthosite (An) content of plagioclases within clast 12 is relatively low (An 92.8), while the An in other clasts is relatively uniform (An_{95.4–97.2}, Table 1, Figure 4). The composition range of olivine is wide (Fo_{67.6–80.7}, Raman spectrum is shown in Figure 3). A variety of mineral fragments of different sizes (Figure 2(a-2)) are also found in some of the clasts, consisting mainly of plagioclase, with small amounts of chromite (TiO₂ = 1.61 wt%, Al₂O₃ = 16.0 wt%, Table 1) and spinel. The plagioclase fragments are pseudo-minerals which retained their original idiomorphic morphology, and they are formed through the accumulation of a large number of plagioclase microcrystals (2 to 5 μm) (Figure 2(a-3), Raman data are shown in Figure 3) (This feature is widely present in NWA 13120 and will be described in detail in Section 3.2). Because of the difference in the size and quantity of plagioclase fragments, the modal abundances of each mineral and the bulk rock composition of the clasts are different. The bulk-rock composition data of clasts No. 01, 02, 04, and 16 indicate that they are rich in aluminum (Al₂O₃ = 28.4–29.4 wt%) and are anorthositic [4] (Table 4). The modal abundance of plagioclase, olivine and vesicles is 63.58 to 79.42 vol%, 13.66 to 33.52 vol% and 1.44 to 6.99 vol%, respectively. The average ratio of modal abundance of plagioclase to olivine is 3.8 (2.4 to 6.8).

The second type of CIM clasts include a total of 3 pieces (shown in blue in Figure 1), and the corresponding numbers are 10, 107 (Figure 2b), and 108. This type of clast has the following characteristics: (1) there is a large number of vesicles ranging from 13.8 to 30.1 vol%, with a size variation from tens of microns to several millimeters. (2) The basaltic component (Figure 2(b-2)) consists of pyroxene and plagioclase with an ophitic to subophitic texture. (3) The pyroxenes are all clinopyroxenes (Raman spectrum is shown in Figure 3) with noticeable compositional zoning (Figure 2(b-2)). The pyroxene core is rich in Mg, and the edge is narrow and rich in Fe. The core and edge of pyroxene in clast No. 10 is $\text{Fs}_{15.9}\text{En}_{56.1}\text{Wo}_{28.1}$, and $\text{Fs}_{74.7}\text{En}_{4.08}\text{Wo}_{21.3}$, respectively. The core and edge of pyroxene in clast No. 107 is $\text{Fs}_{19.0}\text{En}_{75.0}\text{Wo}_{5.9}$, and $\text{Fs}_{27.4}\text{En}_{50.0}\text{Wo}_{22.6}$, respectively. The core and edge of pyroxene in clast No. 108 is $\text{Fs}_{24.9}\text{En}_{59.7}\text{Wo}_{15.4}$, and $\text{Fs}_{50.7}\text{En}_{19.8}\text{Wo}_{29.4}$, respectively. (Table 2, Figure 6). (4) There is chromite in the clasts (clast No. 10, $\text{TiO}_2 = 4.90\text{--}5.26$, $n = 2$). (5) In addition to the basaltic components, it also shows an olivine-plagioclase assemblage with a poikilitic-like texture (Figure 2(b-3)). (6) The plagioclases ($\text{An}_{87.4\text{--}89.7}$) in the basaltic components are more enriched in Na than the plagioclases ($\text{An}_{94.8\text{--}97.0}$) in poikilitic-like texture.

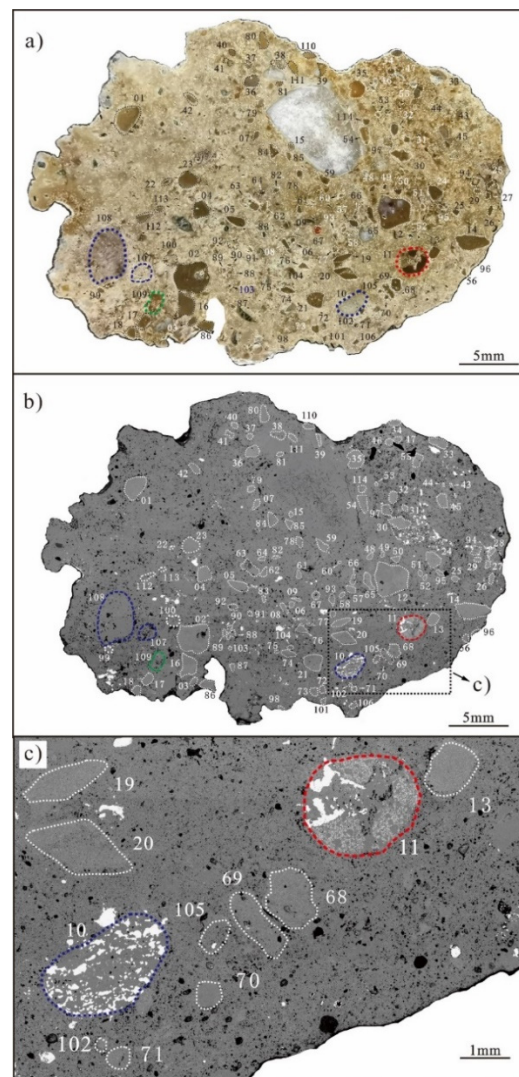


Figure 1. Reflected light image (a) and backscattered electron image (b,c) of the lunar breccia meteorite NWA 13120. Crystalline impact melt clasts larger than 300 μm , the first type: white circles, 105 pieces; the second type: blue circles, 3 pieces (No. 10, 107, and 108); the third type: green circle, 1 piece (No. 109); the fourth type: red circle, 1 piece (No. 11).

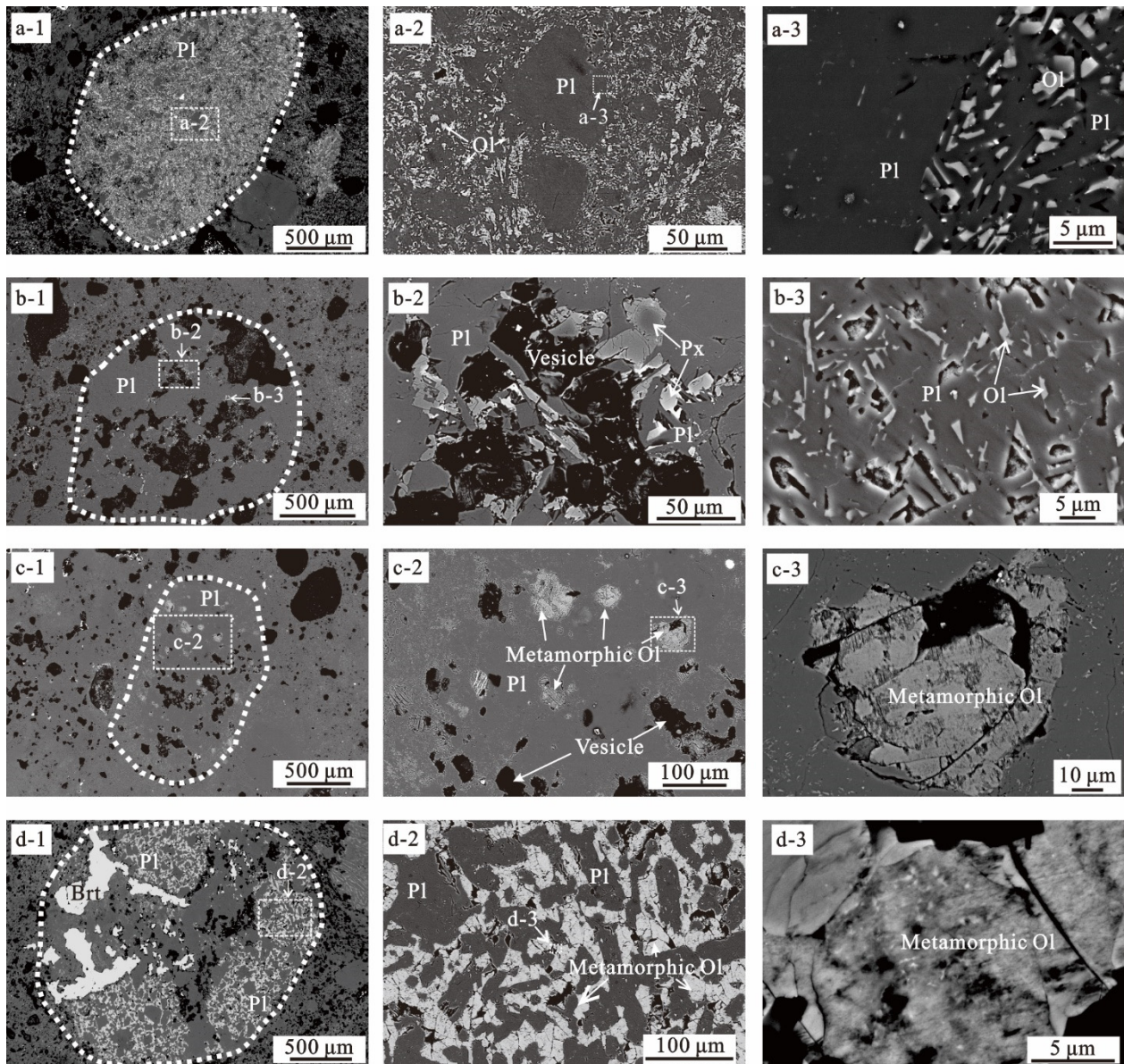


Figure 2. Backscattered electron images of four types of crystalline impact melt clasts. (a). The first type, clast 01; (a-1,a-2): pseudo-plagioclase (Pl) mineral clasts; (a-3): there seems to be the accumulation of a large number of plagioclase microcrystals in the left, the poikilitic-like texture of plagioclase-olivine (Ol) on the right. (b). The second type, clast 107; (b-1): with a large number of vesicles; (b-2): with the basaltic component, the pyroxenes (Px) show chemical zoning; (b-3): the poikilitic-like texture of plagioclase-olivine, the amount of olivine is less than that in the first type. (c). The third type, clast 109; (c-1): a large number of olivine fragments; (c-2,c-3): metamorphic olivine. (d). The fourth type, clast 11; (d-1): the breccia consists of three clasts, and some of the vesicles are filled with barite (Brt); (d-2): an enlarged image of breccia showing the gabbro-like texture of plagioclase and olivine; (d-3): metamorphic olivine.

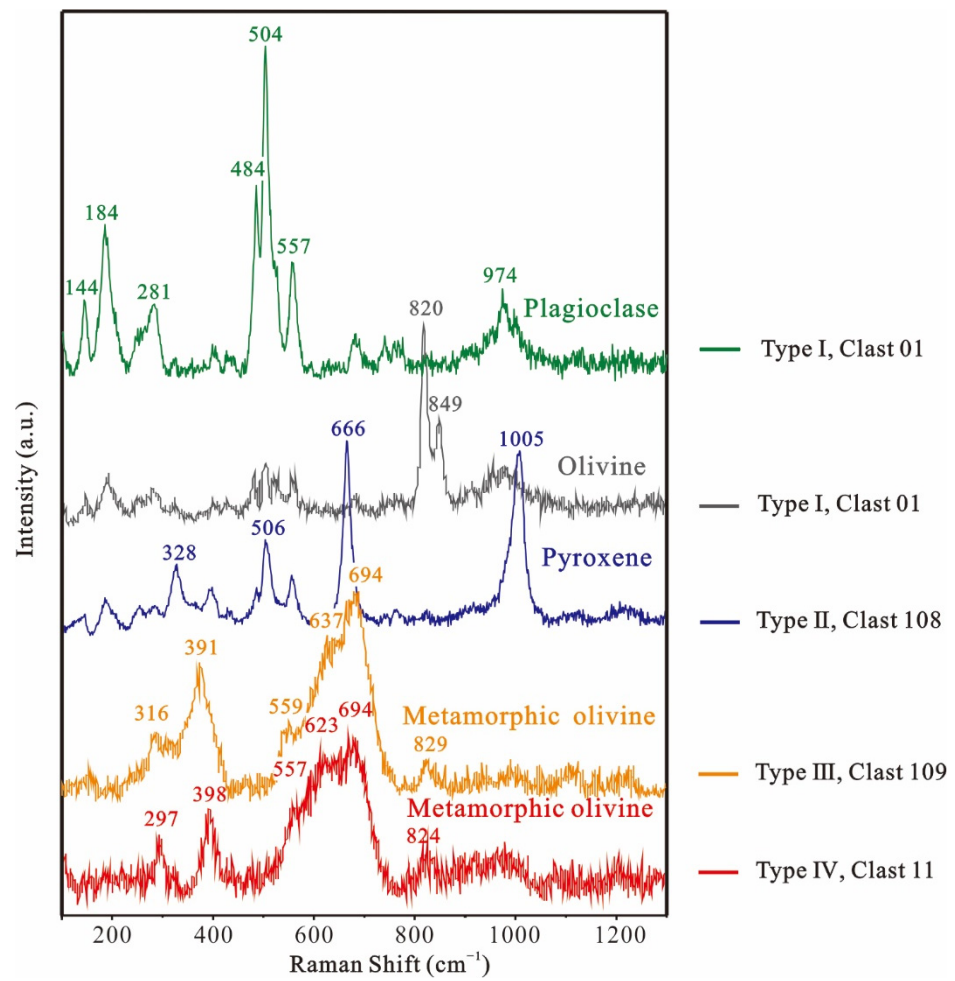


Figure 3. Raman spectra of minerals in different types of crystalline impact melt clasts. Green: Plagioclase microcrystals in plagioclase fragments in first type of clast (No. 01). Gray: Olivine with poikilitic-like texture in the first type of clast (No. 01). Blue: zoned pyroxene in the second type of clast (No. 108). Orange: Metamorphic olivine in the third type of clast (No. 109). Red: Metamorphic olivine in the fourth type of clast (No. 11).

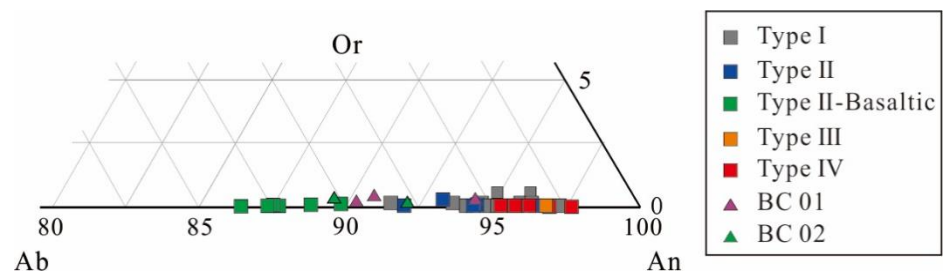


Figure 4. Plagioclase composition in different types of CIM clasts and basaltic clasts.

Table 1. Compositions of representative minerals in first type of crystalline impact melt clasts.

Clast	1		2		4		5		6		7		
	Ol	Pl	Ol	Pl	Ol	Pl	Ol	Pl	Chr	Ol	Pl	Ol	Pl
<i>n</i>	4	3	3	3	7	4	4	5	1	4	5	4	3
SiO ₂	38.81	44.07	38.72	44.3	37.2	42.91	37.72	44.34	0.59	38.32	42.47	37.43	42.28
TiO ₂	b.d.	0.03	0.03	0.05	0.09	0.15	0.05	0.16	1.61	0.03	0.36	0.05	0.07
Al ₂ O ₃	0.07	34.82	0.54	35.32	1.02	34.38	1.02	32.03	16.02	1.14	35.88	0.26	35.38
Cr ₂ O ₃	0.25	b.d.	0.24	0.05	0.26	0.01	0.3	0.06	47.2	0.3	b.d.	0.2	b.d.
FeO	20.22	0.55	21.79	0.51	26.52	0.81	23.46	2.09	27.17	19.79	0.43	25.32	0.37
MnO	0.25	0.02	0.27	0.06	0.31	0.01	0.29	0.05	0.32	0.28	0.01	0.32	0.02
MgO	39.04	0.21	37.22	0.24	32.96	0.36	34.82	1.22	5.04	38.34	0.16	34.41	0.19
CaO	0.44	19.92	0.62	19.18	0.95	19.68	0.99	19.19	0.73	1.07	20.21	0.54	19.72
Na ₂ O	0.01	0.31	0.01	0.33	0.02	0.42	0.01	0.48	b.d.	b.d.	0.46	0.01	0.5
K ₂ O	b.d.	0.01	0.01	b.d.	0.01	0.03	0.02	0.02	b.d.	b.d.	b.d.	b.d.	0.01
P ₂ O ₅	b.d.	b.d.	0.01	0.04	0.03	0.01	0.02	0.02	0.01	0.04	0.01	0.01	0.01
Total	99.09	99.94	99.46	100.08	99.37	98.77	98.7	99.66	98.69	99.31	99.99	98.55	98.55
Oxygen Cations	4	8	4	8	4	8	4	8	4	4	8	4	8
Si	1.009	2.048	1.010	2.049	0.996	2.024	1.002	2.083	0.020	0.994	1.979	1.005	1.996
Ti	-	0.001	0.001	0.002	0.002	0.005	0.001	0.006	0.041	0.001	0.013	0.001	0.002
Al	0.002	1.907	0.017	1.925	0.032	1.911	0.032	1.773	0.634	0.035	1.971	0.008	1.968
Cr	0.005	-	0.005	0.002	0.006	0.000	0.006	0.002	1.252	0.006	0.000	0.004	0.000
Fe	0.440	0.021	0.475	0.020	0.594	0.032	0.521	0.082	0.762	0.429	0.017	0.569	0.015
Mn	0.006	0.001	0.006	0.002	0.007	0.000	0.007	0.002	0.009	0.006	0.000	0.007	0.001
Mg	1.513	0.015	1.447	0.017	1.316	0.025	1.379	0.085	0.252	1.482	0.011	1.377	0.013
Ca	0.012	0.992	0.017	0.951	0.027	0.995	0.028	0.966	0.026	0.030	1.009	0.016	0.997
Na	0.001	0.028	0.001	0.030	0.001	0.038	0.001	0.044	-	-	0.042	0.001	0.046
K	-	0.001	0.000	-	0.000	0.002	0.001	0.001	-	-	-	-	0.001
P	-	-	0.000	0.002	0.001	0.000	0.000	0.001	0.000	0.000	0.000	0.000	0.000
Total	2.99	5.01	2.98	5.00	2.98	5.03	2.98	5.04	3.00	2.98	5.04	2.99	5.04
Fe/Mn	79.1 (70.1–92.5)		78.6 (67.5–99.2)		85.6 (72.7–107.3)		83.1 (64.0–101.2)			70.1 (65.4–84.1)		79.8 (72.8–91.1)	
Fo	77.5 (74.4–80.1)		75.3 (74.3–76.0)		68.9 (64.0–76.9)		72.5 (71.5–73.8)			77.5 (76.4–79.0)		70.8 (69.7–73.0)	
An		97.2 (97.0–97.4)		97 (96.8–97.3)		96.1 (94.8–97.2)		95.6 (94.5–96.4)			96 (95.8–96.3)		95.6 (95.5–95.7)
Ab		2.8 (2.6–3.0)		3 (2.7–3.2)		3.7 (2.7–4.5)		4.3 (3.5–5.3)			3.9 (3.6–4.2)		4.4 (4.3–4.4)
Clast	12		13		15		16		17		39		
<i>n</i>	Ol	Pl	Ol	Pl	Ol	Pl	Ol	Pl	Ol	Pl	Ol	Pl	
SiO ₂	3	6	9	5	5	4	3	3	5	3	4	3	
TiO ₂	37.71	42.18	36.88	42.12	37.31	44.39	37.01	44.03	39.04	44.68	37.59	44.91	
Al ₂ O ₃	0.12	0.18	0.17	0.02	0.07	0.01	0.07	0.14	0.02	0.01	0.04	0.05	
Cr ₂ O ₃	1.12	35.62	0.17	35.11	0.82	35.09	1.89	35.19	0.07	35.49	0.19	35.49	
FeO	0.08	b.d.	0.3	0.3	0.24	0.01	0.13	b.d.	0.23	0.01	0.20	b.d.	
MnO	25.5	0.25	23.3	0.59	26.21	0.42	26.69	0.32	17.78	0.37	25.63	0.28	
MgO	0.25	0.02	0.27	0.01	0.27	0.02	0.30	0.03	0.19	b.d.	0.25	b.d.	
CaO	33.61	0.14	37.01	0.34	32.62	0.2	31.28	0.21	41.69	0.16	34.69	0.17	
Na ₂ O	0.93	19.4	0.6	19.61	0.77	19.93	1.51	20.41	0.36	19.81	0.53	19.08	
K ₂ O	0.03	0.82	0.05	0.51	0.02	0.42	0.02	0.38	0.01	0.46	0.01	0.48	
P ₂ O ₅	0.01	0.02	0.02	0.02	0.01	0.02	b.d.	0.01	0.01	0.01	0.01	0.01	
Total	0.03	0.01	0.01	0.01	0.01	0.02	b.d.	0.01	0.02	0.02	0.03	b.d.	

Table 1. Cont.

Clast	12		13		15		16		17		39	
Total	99.39	98.64	98.78	98.35	98.35	100.53	98.9	100.73	99.42	101.02	99.17	100.47
Oxygen Cations	4	8	4	8	4	8	4	8	4	8	4	8
Si	1.003	1.989	0.982	1.995	1.008	2.049	0.997	2.032	1.000	2.050	1.004	2.064
Ti	0.002	0.006	0.003	0.001	0.001	0.000	0.001	0.005	0.000	0.000	0.001	0.002
Al	0.035	1.980	0.005	1.960	0.026	1.909	0.060	1.914	0.002	1.919	0.006	1.923
Cr	0.002	-	0.006	0.000	0.005	0.000	0.003	-	0.005	0.000	0.004	-
Fe	0.567	0.010	0.519	0.023	0.592	0.016	0.601	0.012	0.381	0.014	0.572	0.011
Mn	0.006	0.001	0.006	0.000	0.006	0.001	0.007	0.001	0.004	-	0.006	-
Mg	1.332	0.010	1.468	0.024	1.313	0.014	1.256	0.014	1.592	0.011	1.381	0.012
Ca	0.026	0.980	0.017	0.995	0.022	0.986	0.044	1.009	0.010	0.974	0.015	0.940
Na	0.002	0.075	0.003	0.047	0.001	0.038	0.001	0.034	0.000	0.041	0.001	0.043
K	0.000	0.001	0.001	0.001	0.000	0.001	-	0.001	0.000	0.001	0.000	0.001
P	0.001	0.000	0.000	0.000	0.000	0.001	-	0.000	0.000	0.001	0.001	-
Total	2.98	5.05	3.01	5.04	2.98	5.01	2.97	5.02	3.00	5.01	2.99	4.99
Fe/Mn	99.8 (97.6–101.1)		85.5 (73.3–95.5)		98.1 (87.6–117.6)		89.5 (84.5–96.7)		92.8 (78.6–105.6)		103.4 (84.4–112.5)	
Fo	70.1 (67.5–72.7)		73.9 (70.1–77.2)		68.9 (65.9–70.7)		67.6 (65.4–71.0)		80.7 (78.5–82.5)		70.7 (65.5–75.5)	
An		92.8 (90.9–94.7)		95.4 (95.1–95.8)		96.2 (95.9–96.5)		96.6 (96.1–97.1)		95.9 (95.6–96.0)		95.6 (95.1–96.1)
Ab		7.1 (5.2–8.9)		4.5 (4.0–4.8)		3.7 (3.5–4.0)		3.3 (3.1–3.7)		4 (3.9–4.3)		4.4 (4.1–4.6)

Note: (1) all oxides are given in wt%; (2) Fs, En, Wo, An and Ab are given in mol%; (3) data in parentheses are range values; (4) b.d.—below detection limit.

Table 2. Compositions of representative minerals in different types of crystalline impact melt clasts.

Type	Type 2										Type 3					Type 4			
Clast	10					107					108					109		11	
	Ol	Pl	Basaltic Pl	Basaltic Px	Chr	Ol	Pl	Basaltic Pl	Basaltic Px	Ol	Pl	Basaltic Pl	Basaltic Px	Metamorphic Ol	Ol	Pl	Metamorphic Ol	Ol	Pl
<i>n</i>	3	14	1	24	2	1	1	4	4	1	9	1	13	1	1	1	5	1	4
SiO ₂	38.43	43.82	45.51	49.6	0.03	39.88	44.57	48.49	52.21	37.21	45.5	49.13	49.73	37.96	36.23	43.91	35.41	37.92	42.88
TiO ₂	0.02	0.08	0.02	0.6	5.08	b.d.	0.03	0.03	0.34	0.12	0.04	0.09	0.97	0.08	b.d.	0.02	0.16	0.04	0.15
Al ₂ O ₃	0.32	35.12	33.81	4.56	10.78	0.10	34.63	32.72	2.96	0.09	33.03	28.51	2.89	0.33	1.90	35.56	0.31	0.15	34.38
Cr ₂ O ₃	0.19	0.01	0.01	0.56	45.42	0.18	0.01	0.01	1.1	0.22	0.02	0.06	0.75	0.13	0.25	b.d.	0.22	0.28	0.01
FeO	23.79	0.57	0.51	13.73	34.33	13.28	0.31	0.48	14.31	29.32	0.38	1.19	19.08	21.66	30.38	0.25	31.69	25.21	0.83
NiO	b.d.	0.01	0.01	0.01	0.02	b.d.	0.01	0.01	0.03	0.02	0.01	b.d.	b.d.	b.d.	0.03	0.02	0.02	b.d.	0.02
MnO	0.25	0.02	0.01	0.23	0.29	0.2	b.d.	b.d.	0.27	0.34	b.d.	0.02	0.33	0.19	0.34	b.d.	0.3	0.23	0.01
MgO	35.61	0.2	0.31	14.24	2.37	46.27	0.21	0.43	21.68	32.72	0.21	0.8	13.41	39.16	30.34	0.15	30.37	35.22	0.36
CaO	0.63	19.48	18.29	15.38	0.04	0.28	19.42	17.19	6.76	0.41	19.18	17.18	12.03	0.49	1.43	19.52	0.51	0.47	19.68
Na ₂ O	0.02	0.41	1.15	0.05	0.04	0.02	0.33	1.34	0.04	b.d.	0.57	1.36	0.05	0.02	b.d.	0.35	0.02	0.02	0.42
K ₂ O	0.02	0.02	0.02	0.01	b.d.	0.01	0.01	0.01	b.d.	b.d.	0.01	0.03	b.d.	0.01	0.01	0.01	0.03	0.01	0.03
P ₂ O ₅	0.01	0.01	0.01	0.02	0.01	b.d.	b.d.	b.d.	b.d.	0.01	0.05	b.d.	0.02	0.03	0.02	b.d.	0.01	0.07	0.01
Total	99.29	99.75	99.66	98.99	98.41	100.22	99.53	100.71	99.7	100.46	99	98.37	99.26	100.06	100.9	99.8	99.05	99.62	98.78
Oxygen Cations	4	8	8	6	4	4	8	8	6	4	8	8	6	4	4	8	4	4	8
Si	1.014	2.039	2.111	1.880	0.001	0.992	2.071	2.208	1.918	0.998	2.125	2.301	1.911	0.986	0.975	2.037	0.980	1.005	2.023
Ti	0.000	0.003	0.001	0.017	0.135	-	0.001	0.001	0.009	0.002	0.001	0.003	0.028	0.002	-	0.001	0.003	0.001	0.005
Al	0.010	1.926	1.848	0.204	0.449	0.003	1.897	1.756	0.128	0.003	1.818	1.574	0.131	0.010	0.060	1.944	0.010	0.005	1.912
Cr	0.004	0.000	0.000	0.017	1.269	0.004	0.000	0.032	0.005	0.001	0.002	0.023	0.003	0.005	-	0.005	0.006	0.000	0.000
Fe	0.525	0.022	0.020	0.435	1.014	0.276	0.012	0.018	0.440	0.658	0.015	0.047	0.613	0.470	0.684	0.010	0.734	0.559	0.033
Ni	-	0.000	0.000	0.000	0.001	-	0.000	0.001	0.000	0.000	-	-	-	-	0.001	0.000	0.000	-	0.001
Mn	0.006	0.001	0.000	0.007	0.009	0.004	-	-	0.008	-	0.001	0.011	0.004	0.008	-	0.007	0.005	0.000	0.000
Mg	1.401	0.014	0.021	0.805	1.125	1.717	0.015	0.029	1.188	1.309	0.015	0.056	0.768	1.516	1.217	0.010	1.253	1.391	0.025
Ca	0.018	0.971	0.909	0.625	0.002	0.007	0.967	0.839	0.266	0.012	0.960	0.862	0.495	0.014	0.041	0.970	0.015	0.013	0.995
Na	0.001	0.037	0.103	0.004	0.003	0.001	0.030	0.118	0.003	-	0.052	0.123	0.004	0.001	-	0.031	0.001	0.001	0.038
K	0.001	0.001	0.001	0.000	-	0.000	0.001	0.001	-	-	0.001	0.002	-	0.000	0.000	0.001	0.001	0.000	0.002
P	0.000	0.000	0.000	0.001	0.000	-	-	-	0.000	0.002	-	-	0.001	0.001	0.000	0.000	0.000	0.002	0.000
Total	2.98	5.01	5.02	3.99	3.01	3.00	4.99	4.97	3.99	3.00	4.99	4.97	3.98	3.01	2.99	5.01	3.01	2.99	5.04
Fe/Mn	92.8 (87.4–96.9)			56.9 (38.1–111.4)		66.5		53.5 (40.0–65.6)		86.3		56.6 (34.3–84.2)	115.7	88.6		101.9 (89.6–113.8)	107.3		
Fo	72.7 (72.0–73.8)					86.1				66.6			76.3	64		64.8 (66.2–67.8)	71.3		
Mg [#]				65.8 (5.2–74.0)				72.2 (64.6–76.8)				94.8 (92.0–96.6)	87.4			56.2 (29.7–72.5)			
An		96.3 (94.6–97.7)	89.7				97	87.6 (86.4–88.8)			94.8 (92.0–96.6)					96.8			96.3 (95.2–97.7)
Ab		3.65 (2.19–5.65)	10.2				3	12.4 (11.2–13.5)			5.13 (3.31–8.0)	12.5			3.17				3.6 (2.3–4.7)
Fs				23.7 (14.6–74.7)				23.3 (19.0–27.4)					32.8 (17.8–50.7)						
En				42.9 (4.08–56.1)				62.4 (50.0–75.0)					40.7 (19.8–59.7)						
Wo				33.4 (15.4–41.9)				14.2 (5.9–22.6)					26.5 (14.4–40.6)						

Note: (1) all oxides are given in wt%; (2) Fs, En, Wo, An and Ab are given in mol%; (3) Mg[#] equals with atomic ratios of Mg/(Mg + Fe); (4) data in parentheses are range values; (5) b.d.—below detection limit.

The third type of CIM clast is numbered 109 (shown in green in Figures 1 and 2c). The main mineral in this clast is plagioclase ($An_{96.8}$, Table 2, and Figure 4). This clast differs from the first type in that it contains a small fraction of “olivine” fragments ($Fo_{76.3}$) (see clast No. 109 in Table 2). These fragments are euhedral to subhedral are 40 to 130 μm in size (Figure 2(c-3)). Although the chemical composition and ion number of this fragment is the same as that for olivine, the Raman data indicates that the crystal structure of these olivine fragments was likely metamorphic. Except for the metamorphic olivine fragments, it has a poikilitic-like texture similar to the first type. Compared with metamorphic olivine fragments, olivine in the poikilitic-like texture is more depleted in Mg but enriched in Fe ($Fo = 64$ mol%, Table 2). In addition, the plagioclase abundance in the poikilitic-like texture of this CIM clast is much higher (about 88 vol%) than that of the first type.

The fourth type of CIM clast is numbered 11 (shown in red in Figures 1 and 2d), which contains three lithic fragments with impact melt matrix (Figure 2(d-1)). The three lithic fragments in clast No. 11 are composed of olivine and plagioclase with a gabbro-like texture (Figure 2(d-2)). These olivines in lithic fragments, which account for average 40.6 vol% in each fragments, were metamorphic, and have similar Raman data to the metamorphic olivines in the third type (Figures 2(d-3) and 4). The plagioclase (30 to 120 μm) in lithic fragments, which retain the original plagioclase idiomorphic morphology, is composed of many plagioclase microcrystals. The matrix in the clast No. 11 is composed of plagioclase fragments and a plagioclase-olivine assemblage with a poikilitic-like texture. The composition of all plagioclase in clast No. 11 is uniform, all of which are anorthite ($An_{95.9-96.5}$). Olivine in the poikilitic-like matrix of the clast (Ol of clast No. 11 in Table 2) is different from the metamorphic olivine in both composition ($Fo = 64.8$ and 71.3 , respectively) and structure (Figure 2d). In clast No. 11, plagioclase accounts for 56.9 vol%, olivine 24.9 vol%, and weathered minerals (barite) and vesicles are 11.3 vol% and 6.9 vol%, respectively.

3.1.2. Basaltic Clasts

Two basaltic clasts were observed in NWA 13120, numbered as basaltic clast 01, and basaltic clast 02 (abbreviated as BC 01 and BC 02, Figure 5a,b). The clasts are about $130 \mu\text{m} \times 60 \mu\text{m}$ and $110 \mu\text{m} \times 40 \mu\text{m}$ in size, respectively. The boundary between the two clasts and the matrix is fuzzy; additionally, microcrystal plagioclase with a size of 2 to 5 μm can be seen at the boundary. The dominant minerals here are pyroxene and plagioclase. The content of plagioclase and pyroxene in BC 01 is about 38 vol% and 58 vol%, respectively. The content of plagioclase and pyroxene in BC 02 is about 47 vol% and 49 vol%, respectively. The plagioclase is almost euhedral in the two clast pieces. The plagioclase grains in the center are larger (8 to 15 μm), while those near the edge are smaller (3 to 8 μm), all of which are anorthite ($An_{89.5-94.6}$, $n = 5$, Table 3). The pyroxenes are 15 to 30 μm in size, all of which are clinopyroxene with significantly compositional zoning (Figures 5c and 6). In BC 01, the pyroxene is $Fs_{15.1-69.7}En_{7.5-41.4}Wo_{22.4-46.1}$, averaging $Fs_{33.0}En_{32.3}Wo_{34.7}$, with $Mg^{\#}$ ranging from 9.76 to 71.9 (averaging 51.8). The plagioclase is $An_{90.3-94.6}$ and is more enriched in Na than the matrix (Figure 5c,d). The pyroxene in BC 02 is $Fs_{27.8-45.3}En_{29.0-47.2}Wo_{25.0-25.7}$, averaging $Fs_{36.6}En_{38.1}Wo_{25.3}$, with $Mg^{\#}$ ranging from 39.0 to 63.0 (averaging 51.0). The plagioclase is $An_{89.5-92.1}$.

3.2. Mineral Fragments and Matrix

The mineral fragments in NWA 13120 are mainly plagioclase, with small amounts of pyroxene, olivine, chromite, ilmenite, spinel, and secondary Earth minerals (chiefly barite, with a small amount of calcite, quartz, potassium plagioclase, and iron oxides). The size of the plagioclase fragments (including plagioclase greater than 50 μm in lithic clasts) ranges from 100 μm to 2 mm, with the largest being 8 mm (Figures 1 and 7(b-1)). These plagioclase fragments are similar to that in lithic clasts, all of which are composed of a large number of fine-grained (2 to 5 μm) plagioclases with different oriented, while their original idiomorphic morphology has been retained, and are continuous with the matrix (Figure 7(b-2–b-4)). These microcrystal plagioclases and mafic intergrowth minerals

(which are too small to identify in terms of their mineral phase) form a poikilitic-like texture resembling lithic clasts and matrix (Figure 7(b-3,b-4)). The anorthite content of plagioclase is uniform ($An_{92.2-97.9}$, $n = 11$), but no maskelynite was found. The pyroxenes are subhedral with compositional zoning, ranging in size from 50 to 100 μm and all the pyroxenes are clinopyroxenes. The composition of the pyroxene fragments varies greatly ($Fs_{5.4-32.6}En_{37.7-49.4}Wo_{29.6-48.7}$, $Mg^\# = 53.6-89.5$, $n = 8$). Raman data shows that the structures of the edge and core of these large-grain olivines fragments ($>100 \mu m$) are different, and the edges were metamorphic similar to the olivine fragments in the third type and fourth type CIM clasts (Figure 7(c-1,c-2)). The smaller olivine fragments (ranging in size from 50 to 80 μm) were all metamorphic.

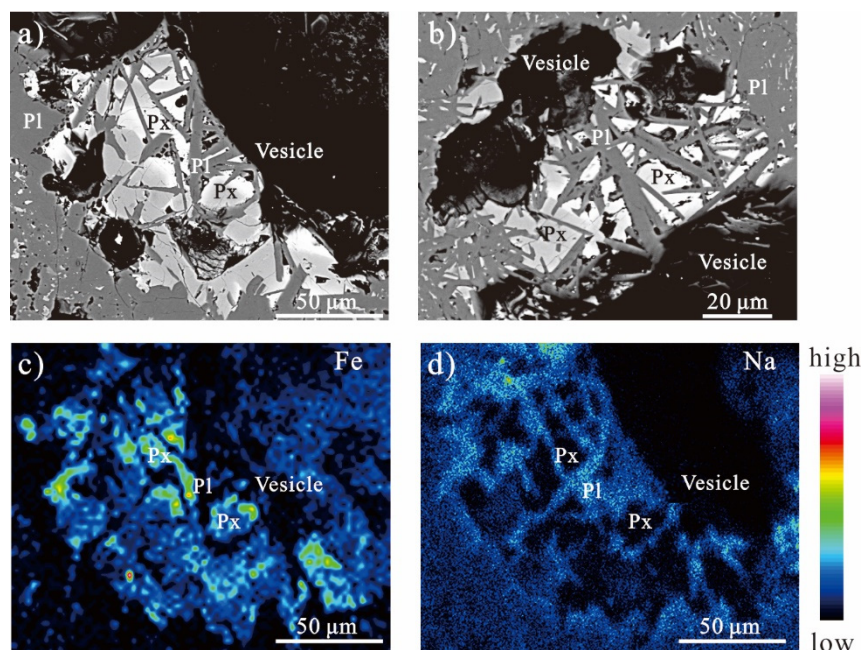


Figure 5. Backscatter electron images of two basaltic clasts and scanning results for Fe and Na. (a) Backscatter image of BC 01. (b) Backscatter image of BC 02. (c) Distribution map of Fe content in BC 01, showing that pyroxene (Py) has compositional zoning. (d) Distribution map of Na content in BC 01, showing that the clast is more enriched in Na than the matrix.

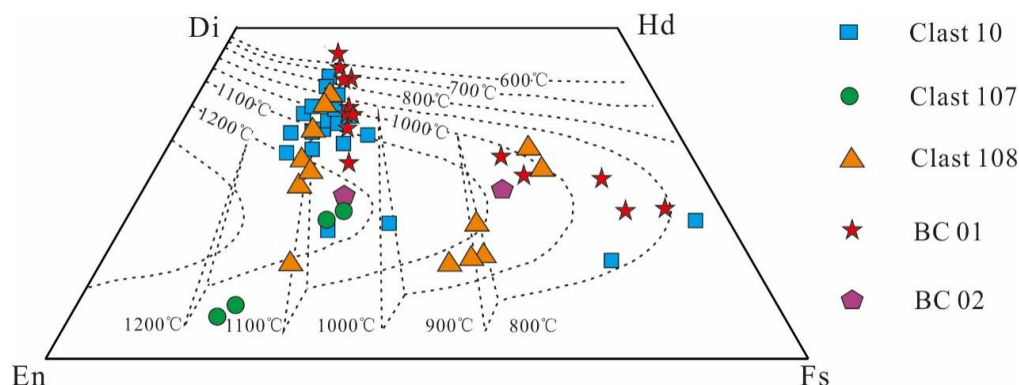


Figure 6. Composition of pyroxene in second types of CIM clasts and basaltic clasts. Pyroxene geothermometer after [18].

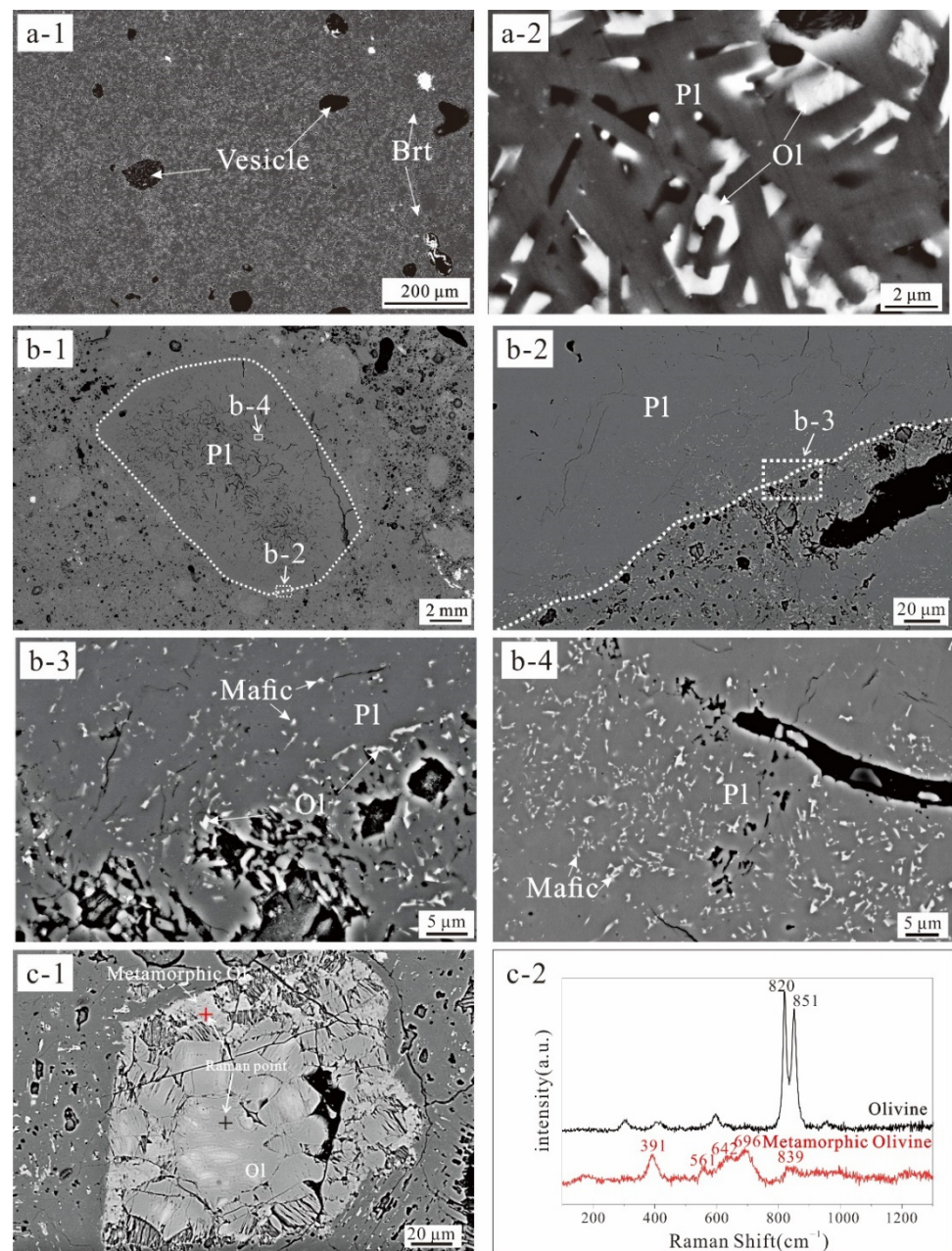


Figure 7. Backscatter electron images and Raman data of the matrix and mineral fragments. (a): the matrix. (a-1): Vesicles in the matrix and some are filled with barite (Brt); (a-2): Enlarged photograph of (a-1), showing that the matrix is composed of plagioclase and olivine microcrystals with a poikilitic-like texture. (b-1): The biggest plagioclase mineral fragment (about 8 mm) in NWA 13120; (b-2): Enlarged photograph of (b-1), showing the edge of plagioclase fragment; (b-3): Enlarged photograph of (b-2), showing that the plagioclase microcrystals in plagioclase fragments and matrix are continuous and the boundary is not clear; (b-4): Enlarged photograph of the core of plagioclase in (b-1), showing microcrystal plagioclases and mafic minerals with a poikilitic-like texture. (c-1): The edge of the olivine mineral fragment was metamorphic and the different colored crosses correspond to the Raman data in (c-2).

Table 3. Compositions of pyroxenes (Px) and plagioclases (Pl) in basaltic clasts.

	BC 01		BC 02	
	Px	Pl	Px	Pl
<i>n</i>	14	3	2	2
SiO ₂	50.02	47.86	49.39	47.48
TiO ₂	1.01	0.07	0.5	0.02
Al ₂ O ₃	3.27	32.01	2.31	31.67
Cr ₂ O ₃	0.64	0.01	0.24	0.01
FeO	19.01	1.3	21.4	1.13
NiO	0.02	0.01	0.02	0.03
MnO	0.32	0.03	0.33	0.03
MgO	10.72	0.45	12.59	0.52
CaO	15.88	18.67	11.61	17.29
Na ₂ O	0.04	0.87	0.02	0.95
K ₂ O	0.01	0.05	b.d.	0.03
P ₂ O ₅	0.03	0.02	0.02	0.03
Total	100.97	101.35	98.43	99.19
Oxygen Cations	6	8	6	8
Si	1.907	2.186	1.932	2.205
Ti	0.029	0.002	0.015	0.001
Al	0.147	1.723	0.107	1.733
Cr	0.019	0.000	0.007	0.000
Fe	0.606	0.050	0.700	0.044
Ni	0.001	0.000	0.001	0.001
Mn	0.010	0.001	0.011	0.001
Mg	0.609	0.031	0.734	0.036
Ca	0.649	0.914	0.487	0.860
Na	0.003	0.077	0.002	0.086
K	0.000	0.003	-	0.002
P	0.001	0.001	0.001	0.001
Total	3.98	4.99	4.00	4.97
Fe/Mn	55.5 (37.3–72.9)		65.0 (50.3–79.8)	
Mg [#]	51.8 (9.76–71.9)		51.0 (39.0–63.0)	
Fs	33.0 (15.1–69.7)		36.6 (27.8–45.3)	
En	32.3 (7.5–44.2)		38.1 (29.0–47.2)	
Wo	34.7 (22.4–46.1)		25.3 (25.0–25.7)	
An		91.9 (90.3–94.6)		90.8 (89.5–92.1)
Ab		7.83 (5.12–9.53)		9.02 (7.81–10.2)

Note: (1) all oxides are given in wt%; (2) Fs, En, Wo, An and Ab are given in mol%; (3) Mg[#] values equals with atomic ratios of Mg/(Mg + Fe); (4) data in parentheses are range values.

The matrix is composed primarily of plagioclase and olivine (1 to 5 μm) with a poikilitic-like texture and a small amount of fine-grained (less than 50 μm) pyroxene, ilmenite, and chromite. The plagioclases are similar to the plagioclase microcrystals in lithic clasts (Figure 7(a-2)). The modal abundance ratio of plagioclase and olivine from the poikilitic-like texture is about 4.2:1. The lunar regolith components (agglutinates and glass spheres) were not found in the matrix. The boundary between the matrix and clasts is continuous and unclear, and irregular plagioclases can be seen at the boundary. A large number of vesicles are distributed unevenly across the matrix. The vesicle size ranges from a few microns to a few millimeters, and the modal abundance is about 6 vol% (Figure 7(a-1)). Some of the vesicles are filled with secondary minerals, mainly barite (BaSO₄).

3.3. Bulk Composition

The major chemical components in NWA 13120 are shown in Table 4. Because of the presence of a large number of micron-scale vesicles, the total content data by electron probe analysis is relatively low (94.5 wt%). We have thus normalized the original data and the results (Table 4). The following discussion refers to both the normalized EPMA defocus data and the fusing bead data. It can be seen from Table 4 that the bulk rock is anorthositic, enriched in aluminum ($\text{Al}_2\text{O}_3 = 30.7$ to 31.9 wt%), and poor in mafic composition ($(\text{MgO} + \text{FeO})/\text{Al}_2\text{O}_3 = 0.13$ to 0.15).

Table 4. Bulk compositions of some clasts, matrix, and NWA 13120 (wt%).

	First Type of Crystalline Impact Melt Clasts				Matrix	NWA 13120	
	Clast 01	Clast 02	Clast 04	Clast 16		Normalization	EPMA-Molten Bead
	EPMA-Defocus						
<i>n</i>	11	7	5	5	11	34	10
SiO ₂	42.9 ± 2.32	43.0 ± 1.7	42.6 ± 0.61	42.5 ± 2.4	43.1 ± 3.6	41.3 ± 3.8	43.7
TiO ₂	0.24 ± 0.03	0.24 ± 0.04	0.24 ± 0.00	0.23 ± 0.04	0.26 ± 0.05	0.27 ± 0.08	0.29
Al ₂ O ₃	28.9 ± 1.6	28.7 ± 0.81	29.4 ± 0.32	28.4 ± 1.71	31.4 ± 3.24	30.1 ± 5.52	31.9
Cr ₂ O ₃	0.06 ± 0.01	0.09 ± 0.01	0.11 ± 0.00	0.06 ± 0.01	0.07 ± 0.03	0.07 ± 0.03	0.07
FeO	3.68 ± 0.40	4.47 ± 0.21	3.87 ± 0.13	4.46 ± 0.51	2.34 ± 0.80	2.13 ± 0.70	2.25
MnO	0.05 ± 0.01	0.06 ± 0.01	0.05 ± 0.00	0.05 ± 0.01	0.03 ± 0.02	0.03 ± 0.01	0.03
MgO	3.15 ± 0.20	3.94 ± 0.10	2.67 ± 0.03	4.30 ± 0.30	1.91 ± 0.30	1.75 ± 0.30	1.85
CaO	16.8 ± 0.90	16.4 ± 0.60	17.1 ± 0.20	16.1 ± 1.10	18.9 ± 1.10	18.3 ± 1.40	19.4
Na ₂ O	0.39 ± 0.04	0.42 ± 0.04	0.35 ± 0.02	0.56 ± 0.08	0.41 ± 0.10	0.49 ± 0.10	0.52
K ₂ O	0.03 ± 0.00	0.04 ± 0.00	0.03 ± 0.00	0.04 ± 0.01	0.04 ± 0.02	0.04 ± 0.02	0.04
P ₂ O ₅	0.01 ± 0.00	0.02 ± 0.00	0.02 ± 0.00	0.03 ± 0.00	0.01 ± 0.00	0.02 ± 0.01	0.02
Total	96.2	97.4	96.5	96.7	98.5	94.5	100
Mg [#]	60.4	61.1	55.2	63.2	59.3		59.4
Fe/Mn	72.7	73.6	76.4	80.1	77		74.1
(MgO + FeO)/Al ₂ O ₃	0.24	0.29	0.22	0.31	0.14		0.13

Note: Mg[#] values equals with atomic ratios of Mg/(Mg + Fe).

4. Discussion

4.1. Classification of NWA 13120

From the returned lunar samples by the Apollo, Luna and Chang'E missions and other lunar meteorites, there is abundant information on the composition of lunar material, including the types and distribution of rocks, and the mineral, geochemical, and isotopic composition of the lunar crust (e.g., [3,9,19,20]). The breccia meteorite in this study, NWA 13120 has similar petrological, mineralogical, and geochemical characteristics with the lunar samples and meteorites, indicating that NWA 13120 originated from the Moon: (1) The recrystallized matrix and melted texture indicate that NWA 13120 has undergone a strong shock melting process. (2) The Fe/Mn ratio of mafic minerals in NWA 13120 shows a linear relationship, which is consistent with the Moon, and noticeably different from that of meteorites from other planets, asteroids, or Earth rocks (Figure 8). (3) NWA 13120 contain numerous plagioclases (An ranges from 86 to 98 with an average of 95). The bulk composition shows high content of Al₂O₃ (30.7 to 31.9 wt%) and poor in mafic minerals ($(\text{MgO} + \text{FeO})/\text{Al}_2\text{O}_3 = 0.13$ to 0.15), which is consistent with the typical anorthitic lunar samples [4]. (4) The Fe/Mn ratio of NWA 13120 is 70.1, which is within the range of other anorthosite lunar rocks (60 to 80) [6,21,22].

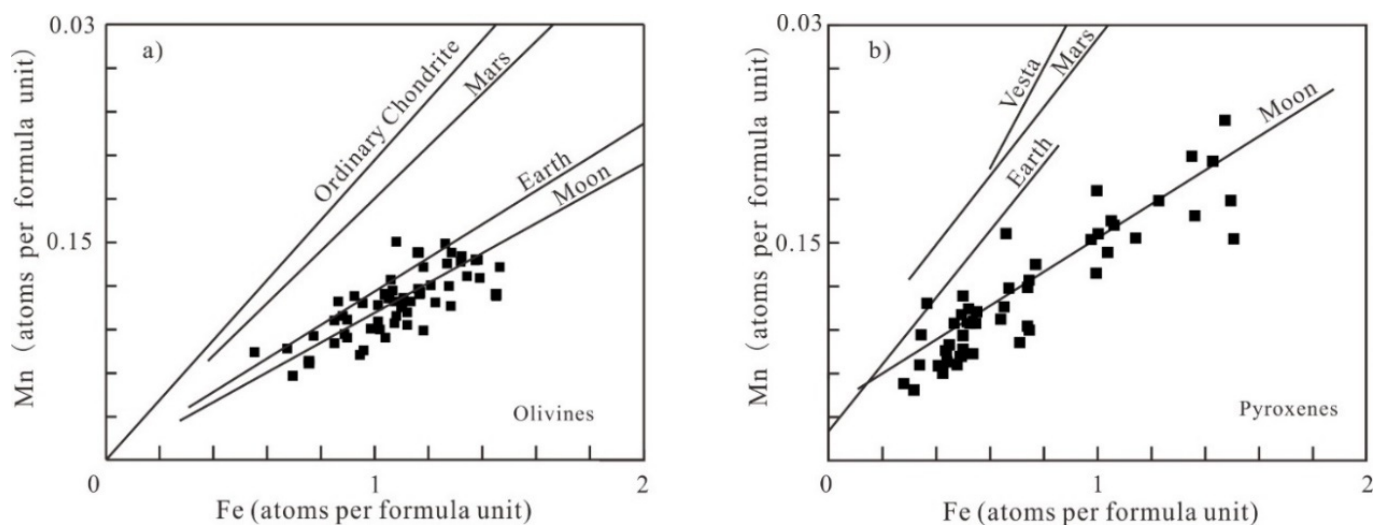


Figure 8. Fe-Mn atomic ratio of olivine (a) and pyroxene (b) in NWA 13120. The atomic numbers of Fe and Mn in olivine and pyroxene show a linear relationship, distributing near the trend line of lunar samples [6], which is different from the materials of other planets, asteroids or Earth rocks.

Agglutinates and glass spherules form during micrometeorite impact on the lunar surface, important components of lunar regolith breccias [23], have not been observed in NWA 13120. Combined with the characteristics of recrystallized shock melt and brecciated texture in NWA 13120, we deduce that the sample is a crystalline impact melt breccia [23] formed by the shock of a celestial body with the Moon. From the chemical composition of NWA 13120, the contents of Al_2O_3 (30.7 to 31.9 wt%) and FeO (2.13 wt%) are similar to those of the Apollo ferrous anorthosite suite (FAN-suite) ($\text{Al}_2\text{O}_3 = 26.5$ to 35.6 wt%, FeO = 0.2 to 6.6 wt% [24,25]), indicating that NWA 13120 may be a crystalline impact melt breccia produced by shock of FAN target material.

4.2. Types of Lithic Clasts in NWA 13120

Crystalline impact melt clasts are widely found in lunar breccias and are the products of lunar shock events (e.g., [4,26]). Because of their complex structure and mineral composition, they were widely studied to distinguish the different properties of such clasts (e.g., [6,13,27]). The petrological and mineralogical characteristics indicate that all the clasts in NWA 13120 are crystalline impact melt rocks. In order to understand the characteristics of the lunar crust revealed by different types of clasts in NWA 13120, we classify and discuss the clasts based on their mineral composition.

In NWA 13120, the first type of crystalline impact melt clasts have similar textures, but widely varying mineral modal abundance and composition. According to the modal abundance values described in Section 3.1.1, the abundance ratio of plagioclase to olivine in the clasts varies greatly from 2.4 to 6.8, belonging to troctolitic anorthosite or anorthosite [28]. Moreover, the $\text{Mg}^\#$ value in this type of clast is high and varies widely from 65.4 to 82.5. In Figure 9, most of these clasts fall in the upper part of the FAN range, with a few falling in the range of Mg-suite. Large amounts of data indicate that highland anorthosite lunar meteorites are more enriched in magnesium than the Apollo FANs samples (e.g., [27,29–32]). NWA 13120 is depleted in incompatible elements (like potassium and phosphorus), which indicates that these clasts are not associated with the Mg-suite. Some studies also show that these Mg-rich components are not from a simple mixture of FAN and Mg-suite rocks [19,33], as well as they were not derived from the same magma chamber due to the large variation of $\text{Mg}^\#$ [32]. Some of the previous studies [32,34] suggest that the primitive magmas in the lunar highlands may be more enriched in Mg than the FAN in Apollo samples, and the primitive crust on the far side of the Moon has a lower degree of evolution and a higher Mg content than on the near side. A new study [35] suggests that the rich Mg is caused

by metasomatism between primitive anorthosite lunar crust and mantle melt. Regardless of the cause, the first type of crystalline impact melt clasts in NWA 13120 have similar textures, which were caused by later events, but the sources of the clasts are diverse from each other and significantly different from those of FAN obtained from Apollo samples.

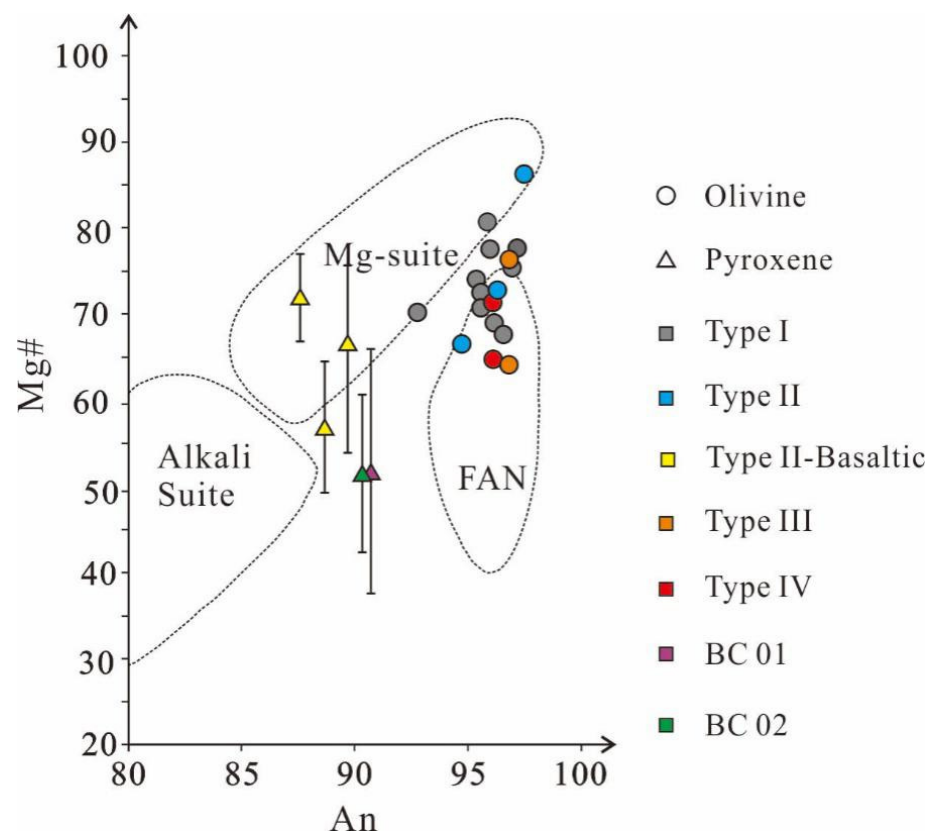


Figure 9. $Mg^{\#}$ value of ferromagnesian minerals versus An value of coexisting plagioclases in clasts after [27]. Symbol shapes indicate mineral types, color in squares indicate rock types.

The second type of crystalline impact melt rock clasts is the only type containing pyroxene. Based on the $Mg^{\#}$ values from the mafic minerals and the An values from the non-basaltic plagioclase, three clasts fall within the range of FAN and the magnesian suite (Figure 9). The pyroxenes in the basaltic components are all clinopyroxene with compositional zones and are usually found in basalt, breccias, and impinged melting rocks; however, these are relatively rare in the highland anorthosite suites and magnesite suites from the Apollo lunar samples [36]. The $Fe^{\#}$ and $Ti^{\#}$ values can reveal the composition of parent magma [37]. The trend lines of $Ti^{\#}$ ($Ti/(Ti + Cr)$) vs. $Fe^{\#}$ ($Fe/(Fe + Mg)$) of pyroxene in different clasts of NWA 13120 are similar to but fall to the left of the Apollo basaltic pyroxene (Figure 10a). This may be because this type of clast is more enriched in Mg than the Apollo samples, the same as the first type of clast. Chromite in this type of clast is more enriched in titanium than in the first type of clast (Tables 1 and 2), indicating that it may be of basaltic origin [36]. Except clast 107 that may have a Very low-Ti basalt origin, the other basaltic clasts are low-Ti basalt origin (Figure 10b). Besides, the composition and texture of two basaltic clasts (BC 01 and BC 02) are similar to those of basaltic components in this type of clast (Figures 9 and 10), are low-Ti basalt origins (Figure 10).

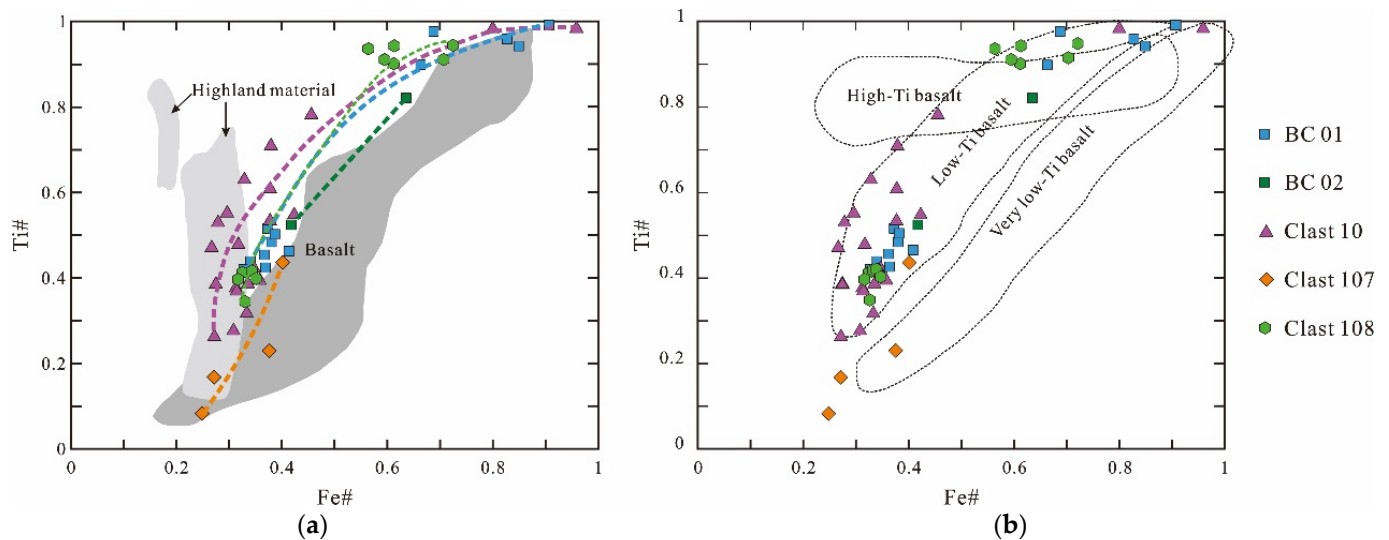


Figure 10. $Ti^{\#}$ ($Ti/(Ti + Cr)$) vs. $Fe^{\#}$ ($Fe/(Fe + Mg)$) of pyroxene in NWA13120 clasts. (a) The relationship between pyroxene in NWA 13120 and basalt and highland material, where the dotted line is the trend of pyroxene composition in different clasts, and the division of highland material and basalt area is according to [38,39]. (b) The relationship between pyroxene in NWA 13120 and basalt with high-Ti, low-Ti, and very low-Ti, the division is according to [40,41].

There is only one clast fragment in the third and fourth types of crystalline impact melt clasts, which is a troctolitic anorthosite. According to the mineral morphology, chemical compositions and Raman spectra, the olivine fragments in these two kinds of clasts have undergone metamorphism. Under high temperature and pressure, the olivine structure will change to the form of wadsleyite or ringwoodite (e.g., [42–44]). As the pressure increases, olivine will be transformed into ahrensite [45], and when the pressure reaches 25 GPa, olivine will be further dissociated into bridgmanite + periclase or wüstite [46]. Although we cannot accurately determine the initial texture of the metamorphic olivine in different types of CIM clasts, as these olivines have similar Raman data, we could infer that the metamorphism was caused by the same shock event. Additionally, the fourth type of crystalline impact melt rock clasts has three lithic fragments, which is unlike the third type. Here, the clasts in fourth type of CIM clast are troctolitic with gabbro-like texture. The clear differences in texture and composition of the two types of clasts indicate that they originated from different sources. Considering that the olivine mineral fragments are also metamorphic, we infer that after the third and fourth types of CIM clasts were brecciated, the shock event (discussed in detail in Section 4.3) caused the olivine to have similar shock metamorphic characteristics.

Lunar breccia is mainly caused by the mixing of different fragments in shock events (e.g., [47–49]). Based on their petrological characteristics, we infer that the diverse types of lithic clasts in NWA 13120 experienced a strong shock event after brecciation. Before this shock event, however, a single shock event or multiple shock events on the lunar FAN highlands mixed together the fragments formed under different conditions at different location, forming the lithic fragments of NWA 13120 with various compositions.

4.3. The Shock Process

4.3.1. In Situ Devitrification and Partial Melting

In NWA 13120, the boundary between the clasts and the matrix is not clear. The texture of the edge and the core of the clasts are the same, and the plagioclase microcrystals along the boundary infiltrate into both the clasts and matrix, indicating the clasts and the matrix were formed at the same time. The pseudo-mineral plagioclase fragments formed by the accumulation of plagioclase microcrystal retain the original morphology (Figure 7(b-3,b-4)), which indicates that they were originally a pure anorthositic melt or glass. These above phenomena indicate that NWA 13120 suffered a strong shock event

that resulted in the devitrification of plagioclase and the formation of a large number of plagioclase microcrystals (similar to the plagioclases described in the literature [12]). In addition, the plagioclase accumulation formed through devitrification have a similar texture to the microcrystalline plagioclase in the matrix and lithic clasts. The devitrification occurred simultaneously in both the clasts and the matrix. This is also supported by the discussion in Section 4.2, where the third and fourth types of CIM rock clasts and olivine in the matrix underwent a consistent metamorphic process during the shock. Therefore, the shock on NWA 13120 applies across the whole rock rather than being local.

The composition of plagioclase (especially in distribution of Na) in the second type of CIM clast and the basaltic clasts is significantly different from that of the matrix (Figure 5). The plagioclase microcrystals in the lithic clasts, matrix and plagioclase mineral fragments have similar textures and diverse chemical compositions in the first type of CIM. All of these phenomenon persuasively demonstrate that NWA 13120 did not melt in a large area after the shock. Therefore, NWA 13120 did not melt in a large area, but underwent in situ devitrification and recrystallization after the shock. The chemical zoning pyroxenes and randomly orientated plagioclases in these clasts indicate that they were crystallized from melt. These clasts, therefore, did not mix with the matrix, that is, the clasts and the matrix were not molten at the same time, but only a small amount of partial melting occurred before the devitrification. That said, the recrystallization of the basaltic components and whole sample took place simultaneously. The reason why the basaltic fragments melted and the other areas of NWA 13120 did not, as has been suggested previously in the literature [12], is that the basaltic fragments contain more pyroxenes. Therefore, in comparison with the entire rock, its amount of Mg[#] is higher, which leads to its lower melting temperature and melting first. The post-shock temperature was not high enough to melt the entire rock. In addition, the partial melting in the basaltic region likely caused more vesicles to be created.

4.3.2. Estimates of Shock Pressure

In NWA 13120, a large number of very fine-grained plagioclase accumulations retain the original euhedral form of plagioclase (Figures 2(a-2,a-3) and 7(b-1–b-3)), which indicates that they were transformed from the solid phase under high pressure. Maskelynite is a diaplectic glass that forms from plagioclase at shock pressures [50]. Combined with Section 4.3.1, we preliminarily determined that these plagioclase accumulations were formed by devitrification of maskelynite. Maskelynite is often used to define the shock pressure on extraterrestrial rocks (e.g., [51,52]). The higher the calcic content of plagioclase, the lower the shock pressure required to transform the plagioclase into maskelynite [53,54]. Plagioclase of An₉₄ composition transforms into maskelynite at shock pressures ≥ 20 GPa [54]. The Raman peak of the metamorphic olivine fragment is considered to be the glass of pyroxene or bridgmanite, which is the product of decomposed olivine [46]. In terms of its morphology, the olivine fragment seems to be slightly different from the decomposed olivine (Figures 2(c-3,d-3) and 7(c-1) compare with Figure 1b in reference [46]). The pressure at which olivine decomposes is 23–25 Gpa [55], which is higher than the pressure formed by maskelynite. Therefore, we can infer that during the shock, the pressure on the entire rock of NWA 13120 was ≥ 20 Gpa, which is the pressure formed by maskelynite. In addition, all small olivines were metamorphic (Figure 2(c-3,d-3)), while the metamorphism of larger olivine fragments only occurred at the mineral edge, and the core still remains with the original crystal structure (Figure 7(c-1,c-2)). This may be related to the difference in pressure conduction between different types of rocks and different minerals [54].

4.3.3. The Shock Metamorphism Process and Parent Rock Characteristics

Olivine has two textures: one is microcrystalline olivine formed by devitrification and forming a poikilitic-like texture with plagioclase, and the other is partially or completely metamorphic olivine. Before brecciation, these two types of olivine must be different in structure. The high pressure experienced by NWA 13120 caused the olivine mineral fragments to undergo metamorphism, but the olivine in the poikilitic-like texture formed

by devitrification was not metamorphic. Therefore, it can be inferred that the devitrification of the entire rock occurred after the high-pressure event.

Based on the above discussion, it can be inferred that: (1) NWA 13120 has undergone devitrification of the entire rock, so all the components with microcrystalline olivine-plagioclase with poikilitic-like texture were previously vitreous. So the parent rock must contain a large number of glass fragments, which are: troctolitic-anorthositic or anorthositic glass (corresponding to the first type of CIM clasts), glass rich in basaltic fragments (corresponding to the second type of CIM clasts), glass rich in olivine mineral fragments (corresponding to the third type of CIM clast) and glass containing troctolite fragments (corresponding to the fourth type of CIM clast). (2) NWA 13120 did not melt in a large area, so the widely developed vesicles in the matrix already existed in the parent rock. Combining the above two points, the parent rock should be a lunar regolith breccia [23] rich in glass fragments.

According to the discussion in Sections 4.3.1 and 4.3.2, during the shock, the high pressures above 20 GPa transformed the plagioclase mineral fragments into maskelynite, and the olivine was also metamorphic. The post-shock peak temperature resulted in partial melting of the basaltic components. As the rock cooled, the melt recrystallized, forming the present basaltic impact melt clasts. At the same time, the heat generated by the shock resulted in the devitrification of the entire rock, the transformation of the maskelynite into a large number of plagioclase microcrystals, the formation of the first type of CIM clasts by the glassy clasts, and the olivine-plagioclase poikilitic-like texture by the anorthosite glass.

5. Conclusions

According to its petrological and mineralogical characteristics, NWA 13120 is a crystalline impact melt breccia produced by the shock of the FAN target materials. The type of lithic clasts in NWA 13120 are mainly of the crystalline impact melt variety, which can be divided into four types: (a) anorthosite with a large amount of olivine-plagioclase poikilitic-like texture, which originated from multiple sources; (b) anorthosite containing low-Ti and very low-Ti basaltic fragments and rich in vesicles; (c) the troctolitic anorthosite containing metamorphic olivine mineral fragments; and (d) the troctolitic anorthosite containing troctolite fragments. Before the latest shock event, NWA 13120 was a lunar anorthosite regolith breccia. The parent rock is composed of glassy lithic clasts of various compositions and mineral clasts embedded in a glassy matrix. The high pressure produced by the shock changed the mineral fragments of plagioclase into maskelynite, and all the olivine fragments were metamorphic. The post-shock temperature led to the melting of basaltic fragments and subsequently caused the devitrification of the whole rock. Meanwhile, maskelynites formed the accumulation of a large number of plagioclase microcrystals. The glass clasts with different compositions were devitrified to form different kinds of crystalline impact melt clasts.

Author Contributions: Writing—original draft preparation, Z.X.; writing—review and editing, Z.X. and B.M.; petrology and chemical compositions data curation, Z.X., C.Z., H.C., L.X. and P.M.R.; visualization, Y.Z. and B.S. All authors will be informed about each step of manuscript processing including submission, revision, revision reminder, etc. via emails from our system or assigned Assistant Editor. All authors have read and agreed to the published version of the manuscript.

Funding: This research was funded by Strategic Priority Research Program of Chinese Academy of Sciences (XDB 41000000), National Natural Science Foundation of China (Grant 41866008; 41776196; 41173077), Guangxi Scientific Base and Talent Special Projects (No. AD1850007), Project funded by China Postdoctoral Science Foundation (2020M673557XB), the National Science and Technology Infrastructure Platform Project (Grant No. 2005DKA21406), Civil Aerospace Pre Research Project (D020302 and D020206), Guangxi Natural Science Foundation (Grant No. 2021GXNSFBA075061), and Key Laboratory of Lunar and Deep Space Exploration, CAS (Grand No. LDSE201907).

Institutional Review Board Statement: Not applicable.

Informed Consent Statement: Not applicable.

Data Availability Statement: Data available on request due to restrictions privacy. The data presented in this study are available on request from the corresponding author.

Acknowledgments: The manuscript has been significantly improved by the constructive reviews by three anonymous reviewers, Xiaojia Zeng, and the academic editors. The experiments were assisted by Yizhi Liu, Jie Wu and Zhenglin Li.

Conflicts of Interest: The authors declare no conflict of interest.

References

- Warren, P.H.; Ulff-Møller, F.; Kallemeyn, G.W. “New” lunar meteorites: Impact melt and regolith breccias and large-scale heterogeneities of the upper lunar crust. *Meteorit. Planet. Sci.* **2005**, *40*, 989–1014. [[CrossRef](#)]
- Qian, Y.; Xiao, L.; Head, J.W.; van der Bogert, C.H.; Hiesinger, H.; Wilson, L. Young lunar mare basalts in the Chang’e-5 sample return region, northern Oceanus Procellarum. *Earth Planet. Sci. Lett.* **2021**, *555*, 116702. [[CrossRef](#)]
- Warren, P.H.; Kallemeyn, G.W. Geochemical investigation of five lunar meteorites: Implications for the composition, origin and evolution of the lunar crust. *Antarct. Meteor. Res.* **1991**, *4*, 91.
- Korotev, R.L. Lunar geochemistry as told by lunar meteorites. *Chem. Erde-Geochem.* **2005**, *65*, 297–346. [[CrossRef](#)]
- Korotev, R.L.; Irving, A.J. Keeping Up with the Lunar Meteorites-2013. *LPI Contrib.* **2013**, *1719*, 1216.
- Joy, K.H.; Nemchin, A.; Grange, M.; Lapen, T.J.; Peslier, A.H.; Ross, D.K.; Zolensky, M.E.; Kring, D.A. Petrography, geochronology and source terrain characteristics of lunar meteorites Dhofar 925, 961 and Sayh al Uhaymir 449. *Geochim. Cosmochim. Acta* **2014**, *144*, 299–325. [[CrossRef](#)]
- Gnos, E.; Hofmann, B.A.; Al-Kathiri, A.; Lorenzetti, S.; Eugster, O.; Whitehouse, M.J.; Villa, I.M.; Jull, A.J.T.; Eikenberg, J.; Spettel, B.; et al. Pinpointing the source of a lunar meteorite: Implications for the evolution of the moon. *Science* **2004**, *305*, 657–659. [[CrossRef](#)]
- Joy, K.H.; Crawford, I.A.; Russell, S.S.; Kearsley, A.T. Lunar meteorite regolith breccias: An in situ study of impact melt composition using LA-ICP-MS with implications for the composition of the lunar crust. *Meteorit. Planet. Sci.* **2010**, *45*, 917–946. [[CrossRef](#)]
- Zeng, X.; Joy, K.H.; Li, S.; Pernet-Fisher, J.F.; Li, X.; Martin, D.J.P.; Li, Y.; Wang, S. Multiple lithic clasts in lunar breccia Northwest Africa 7948 and implication for the lithologic components of lunar crust. *Meteorit. Planet. Sci.* **2018**, *53*, 1030–1050. [[CrossRef](#)]
- Zeng, X.; Li, S.; Joy, K.H.; Li, X.; Liu, J.; Li, Y.; Li, R.; Wang, S. Occurrence and implications of secondary olivine veinlets in lunar highland breccia Northwest Africa 11273. *Meteorit. Planet. Sci.* **2020**, *55*, 36–55. [[CrossRef](#)]
- Miyahara, M.; Kaneko, S.; Ohtani, E.; Sakai, T.; Nagase, T.; Kayama, M.; Nishido, H.; Hirao, N. Discovery of seifertite in a shocked lunar meteorite. *Nat. Commun.* **2013**, *4*, 1–7. [[CrossRef](#)] [[PubMed](#)]
- Cohen, B.A.; James, O.B.; Taylor, L.A.; Nazarov, M.A.; Barsukova, L.D. Lunar highland meteorite Dhofar 026 and Apollo sample 15418: Two strongly shocked, partially melted, granulitic breccias. *Meteorit. Planet. Sci.* **2004**, *39*, 1419–1447. [[CrossRef](#)]
- Meszaros, M.; Hofmann, B.A.; Lanari, P.; Korotev, R.L.; Gnos, E.; Greber, N.D.; Leya, I.; Greenwood, R.C.; Jull, A.J.T.; Al-Wagdani, K.; et al. Petrology and geochemistry of feldspathic impact-melt breccia Abar al’ Uj 012, the first lunar meteorite from Saudi Arabia. *Meteorit. Planet. Sci.* **2016**, *51*, 1830–1848. [[CrossRef](#)]
- Wittmann, A.; Korotev, R.L.; Jolliff, B.L.; Nishiizumi, K.; Jull, A.J.T.; Caffee, M.W.; Zanetti, M.; Irving, A.J. Petrogenesis of lunar impact melt rock meteorite Oued Awlitis 001. *Meteorit. Planet. Sci.* **2019**, *54*, 2167–2188. [[CrossRef](#)]
- Lin, Y.; Kimura, M.; Miao, B.; Dai, D.; Monoi, A. Petrographic comparison of refractory inclusions from different chemical groups of chondrites. *Meteorit. Planet. Sci.* **2006**, *41*, 67–81. [[CrossRef](#)]
- Zeng, X.; Li, S.; Li, X.; Wang, S.; Li, Y. Method for nondestructive measurement of major elements of lunar soil samples. *Bull. Mineral. Petrol. Geochem.* **2015**, *34*, 1282–1286. (In Chinese with English abstract)
- Feng, L.; Lin, Y.; Hu, S.; Xu, L.; Miao, B. Estimating compositions of natural ringwoodite in the heavily shocked Grove Mountains 052049 meteorite from Raman spectra. *Am. Mineral.* **2011**, *96*, 1480–1489. [[CrossRef](#)]
- Lindsley, D.H. Pyroxene thermometry. *Am. Mineral.* **1983**, *68*, 477–493.
- Korotev, R.L.; Jolliff, B.L.; Zeigler, R.A.; Gillis, J.J.; Haskin, L.A. Feldspathic lunar meteorites and their implications for compositional remote sensing of the lunar surface and the composition of the lunar crust. *Geochim. Cosmochim. Acta* **2003**, *67*, 4895–4923. [[CrossRef](#)]
- Qiao, L.; Chen, J.; Xu, L.; Wan, S.; Cao, H.; Li, B.; Ling, Z. Geology of the chang’e-5 landing site: Constraints on the sources of samples returned from a young nearside mare. *Icarus* **2021**, *364*, 114480. [[CrossRef](#)]
- Palme, H.; Spettel, B.; Jochum, K.P.; Dreibus, G.; Weber, H.; Weckwerth, G.; Wanke, H.; Bischoff, A.; Stöffler, D. Lunar Highland Meteorites and the Composition of the Lunar Crust. *Geochim. Cosmochim. Acta* **1991**, *55*, 3105–3122. [[CrossRef](#)]
- Papike, J.; Karner, J.; Shearer, C. Determination of planetary basalt parentage: A simple technique using the electron microprobe. *Am. Mineral.* **2003**, *88*, 469–472. [[CrossRef](#)]
- Stöffler, D.; Knoell, H.-D.; Marvin, U.B.; Simonds, C.H.; Warren, P.H.; Papike, J.J. Recommended classification and nomenclature of lunar highland rocks—A committee report. In *Proceedings of the Conference on Lunar Highlands Crust*; Papike, J.J., Merrill, R.B., Eds.; Pergamon Press: New York, NY, USA, 1980; pp. 51–70.

24. Norman, M.D.; Ryder, G. Geochemical constraints on the igneous evolution of the lunar crust. *Adv. Synth. Catal.* **1980**, *357*, 2939–2943.
25. Wiczorek, M.A.; Jolliff, B.L.; Khan, A.; Pritchard, M.E.; Weiss, B.P.; Williams, J.G.; Hood, L.L.; Richter, K.; Neal, C.R.; Shearer, C.K.; et al. The Constitution and Structure of the Lunar Interior. *Rev. Mineral. Geochem.* **2006**, *60*, 221–364. [[CrossRef](#)]
26. Heiken, G.H.; Vaniman, D.T.; French, B.M. *Lunar Sourcebook: A User's Guide to the Moon*; Cambridge University Press: Cambridge, UK, 1991.
27. Xue, Z.; Xiao, L.; Neal, C.R.; Xu, Y. Oldest high-Ti basalt and magnesian crustal materials in feldspathic lunar meteorite Dhofar 1428. *Geochim. Cosmochim. Acta* **2019**, *266*, 74–108. [[CrossRef](#)]
28. Prinz, M.; Keil, K. Mineralogy, petrology and chemistry of ANT-suite rocks from the lunar highlands. *Phys. Chem. Earth* **1977**, *10*, 215–237.
29. Hudgins, J.A.; Walton, E.L.; Spray, J.G. Mineralogy, petrology, and shock history of lunar meteorite Sayh al Uhaymir 300: A crystalline impact-melt breccia. *Meteorit. Planet. Sci.* **2007**, *42*, 1763–1779. [[CrossRef](#)]
30. Hsu, W.; Zhang, A.; Bartoschewitz, R.; Guan, Y.; Ushikubo, T.; KrñHenbÜHI, U.; Niedergesaess, R.; Pepelnik, R.; Reus, U.; Kurtz, T.; et al. Petrography, mineralogy, and geochemistry of lunar meteorite Sayh al Uhaymir 300. *Meteorit. Planet.* **2008**, *43*, 1363–1381. [[CrossRef](#)]
31. Mercer, C.N.; Treiman, A.H.; Joy, K.H. New lunar meteorite Northwest Africa 2996: A window into farside lithologies and petrogenesis. *Meteorit. Planet. Sci.* **2013**, *48*, 289–315. [[CrossRef](#)]
32. Gross, J.; Treiman, A.H.; Mercer, C.N. Lunar feldspathic meteorites: Constraints on the geology of the lunar highlands, and the origin of the lunar crust. *Earth Planet. Sci. Lett.* **2014**, *388*, 318–328. [[CrossRef](#)]
33. Kent, J.; Brandon, A.; Joy, K.; Peslier, A.; Lapen, T.; Irving, A.; Coleff, D. Mineralogy and petrogenesis of lunar magnesian granulitic meteorite Northwest Africa 5744. *Meteorit. Planet. Sci.* **2017**, *52*, 1916–1940. [[CrossRef](#)]
34. Ohtake, M.; Takeda, H.; Matsunaga, T.; Yokota, Y.; Haruyama, J.; Morota, T.; Yamamoto, S.; Ogawa, Y.; Hiroi, T.; Karouji, Y.; et al. Asymmetric crustal growth on the Moon indicated by primitive farside highland materials. *Nat. Geosci.* **2012**, *5*, 384–388. [[CrossRef](#)]
35. Xu, X.; Hui, H.; Chen, W.; Huang, S.; Neal, C.R.; Xu, X. Formation of lunar highlands anorthosites. *Earth Planet. Sci. Lett.* **2020**, *536*, 116138. [[CrossRef](#)]
36. Papike, J.; Taylor, L.; Simon, S. Lunar minerals. In *Lunar Sourcebook*; Cambridge University Press: New York, NY, USA, 1991; pp. 121–181.
37. Nielsen, R.L.; Drake, M.J. The case for at least three mare basalt magmas at the Luna 24 landing site. *Geochim. Cosmochim. Acta* **1978**, *9*, 419–428.
38. Hill, P.J.; Osinski, G.R.; Banerjee, N.R.; Korotev, R.L.; Nasir, S.J.; Herd, C.D. Petrography and geochemistry of lunar meteorites Dhofar 1673, 1983, and 1984. *Meteorit. Planet. Sci.* **2019**, *54*, 300–320. [[CrossRef](#)]
39. Arai, T.; Warren, P.H.; Takeda, H. Four Lunar Mare Meteorites: Crystallization Trends of Pyroxenes and Spinel. *Meteorit. Planet. Sci.* **1996**, *31*, 877–892. [[CrossRef](#)]
40. Arai, T.; Warren, P.H. Lunar meteorite QUE 94281: Glass compositions and other evidence for launch pairing with Yamato-793274. *Meteorit. Planet. Sci.* **1999**, *34*, 209–234. [[CrossRef](#)]
41. Robinson, K.L.; Treiman, A.H.; Joy, K.H. Basaltic fragments in lunar feldspathic meteorites: Connecting sample analyses to orbital remote sensing. *Meteorit. Planet. Sci.* **2012**, *47*, 387–399. [[CrossRef](#)]
42. Ohtani, E.; Moriawaki, K.; Kato, T.; Onuma, K. Melting and crystal–liquid partitioning in the system Mg₂SiO₄–Fe₂SiO₄ to 25 GPa. *Phys. Earth Planet. Inter.* **1998**, *107*, 75–82. [[CrossRef](#)]
43. Chen, M.; Chen, J.; Xie, X.; Xu, J. A microstructural investigation of natural lamellar ringwoodite in olivine of the shocked Sixiangkou chondrite. *Earth Planet. Sci. Lett.* **2007**, *264*, 277–283. [[CrossRef](#)]
44. Miyahara, M.; Ohtani, E.; Kimura, M.; El Goresy, A.; Ozawa, S.; Nagase, T.; Nishijima, M.; Hiraga, K. Coherent and subsequent incoherent ringwoodite growth in olivine of shocked L6 chondrites. *Earth Planet. Sci. Lett.* **2010**, *295*, 321–327. [[CrossRef](#)]
45. Ma, C.; Tschauner, O.; Beckett, J.R.; Liu, Y.; Rossmann, G.R.; Sinogeikin, S.V.; Smith, J.S.; Taylor, L.A. Ahrensite, gamma-Fe₂SiO₄, a new shock-metamorphic mineral from the Tissint meteorite: Implications for the Tissint shock event on Mars. *Geochim. Cosmochim. Acta* **2016**, *184*, 240–256. [[CrossRef](#)]
46. Miyahara, M.; Ohtani, E.; Ozawa, S.; Kimura, M.; El Goresy, A.; Sakai, T.; Nagase, T.; Hiraga, K.; Hirao, N.; Ohishi, Y. Natural dissociation of olivine to (Mg,Fe)SiO₃ perovskite and magnesiowüstite in a shocked Martian meteorite. *Proc. Natl. Acad. Sci. USA* **2011**, *108*, 5999–6003. [[CrossRef](#)] [[PubMed](#)]
47. Anand, M.; Taylor, L.A.; Neal, C.R.; Snyder, G.A.; Patchen, A.; Sano, Y.; Terada, K. Petrogenesis of lunar meteorite EET 96008. *Geochim. Cosmochim. Acta* **2003**, *67*, 3499–3518. [[CrossRef](#)]
48. Joy, K.H.; Burgess, R.; Hinton, R.; Fernandes, V.A.; Crawford, I.A.; Kearsley, A.T.; Irving, A.J.; EIMF. Petrogenesis and chronology of lunar meteorite Northwest Africa 4472: A KREEPy regolith breccia from the Moon. *Geochim. Cosmochim. Acta* **2011**, *75*, 2420–2452. [[CrossRef](#)]
49. Korotev, R.L. Compositional variation in Apollo 16 impact-melt breccias and inferences for the geology and bombardment history of the Central Highlands of the Moon. *Geochim. Cosmochim. Acta* **1994**, *58*, 3931–3969.

50. Mustard, J.F.; Herd, C.D.K.; Skok, J.R.; Cannon, K.M. Visible-Infrared Reflectance of the Tissint Meteorite: Impact Melt, Maskelynite and Implications for Mars Remote Sensing. In *44th Lunar and Planetary Science Conference*; Lunar and Planetary Institute: Houston, TX, USA, 2013; p. 2771.
51. Rubin, A.E. Maskelynite in asteroidal, lunar and planetary basaltic meteorites: An indicator of shock pressure during impact ejection from their parent bodies. *Icarus* **2015**, *257*, 221–229. [[CrossRef](#)]
52. Stöffler, D.; Ostertag, R.; Jammes, C.; Pfannschmidt, G.; Gupta, P.R.S.; Simon, S.B.; Papike, J.J.; Beauchamp, R.H. Shock metamorphism and petrography of the Shergotty achondrite. *Geochim. Cosmochim. Acta* **1986**, *50*, 889–903. [[CrossRef](#)]
53. Fritz, J.; Wuenemann, K.; Greshake, A.; Fernandes, V.; Boettger, U.; Hornemann, U. Shock Pressure Calibration for Lunar Plagioclase. In *42nd Lunar and Planetary Science Conference*; Lunar and Planetary Institute: Houston, TX, USA, 2011; p. 1196.
54. Stöffler, D.; Hamann, C.; Metzler, K. Shock metamorphism of planetary silicate rocks and sediments: Proposal for an updated classification system. *Meteorit. Planet. Sci.* **2018**, *53*, 5–49. [[CrossRef](#)]
55. Baziotis, I.; Asimow, P.D.; Hu, J.; Ferrière, L.; Ma, C.; Cernok, A.; Anand, M.; Topa, D. High pressure minerals in the Château-Renard (L6) ordinary chondrite: Implications for collisions on its parent body. *Sci. Rep.* **2018**, *8*, 9851. [[CrossRef](#)]